Appl. Phys. B 70 [Suppl.], S5–S12 (2000) / Digital Object Identifier (DOI) 10.1007/s003400000308

Applied Physics B
Lasers
and Optics

Sub-6-fs pulses from a SESAM-assisted Kerr-lens modelocked Ti:sapphire laser: at the frontiers of ultrashort pulse generation

D.H. Sutter[1], L. Gallmann[1], N. Matuschek[1], F. Morier-Genoud[1], V. Scheuer[2], G. Angelow[2], T. Tschudi[2], G. Steinmeyer[1], U. Keller[1]

[1] Ultrafast Laser Physics Laboratory, Institute of Quantum Electronics, Swiss Federal Institute of Technology, ETH Hönggerberg – HPT, 8093 Zürich, Switzerland
(Fax: +41-1/633-1059, E-mail: DirkSutter@alumni.ethz.ch)
[2] Institute for Applied Physics, Hochschulstrasse 6, 64829 Darmstadt, Germany
(Fax: +49-6151/164-123, E-mail: volker.scheuer@physik.th-darmstadt.de)

Received: 7 October 1999/Revised version: 29 February 2000/Published online: 24 May 2000 –

Abstract. Well-characterized pulses in the two-optical-cycle regime are demonstrated using a Kerr-lens modelocked (KLM) Ti:sapphire laser and phase-sensitive diagnostics. The oscillator employs double-chirped mirrors (DCMs) for dispersion compensation, spectral shaping via wavelength-dependent output coupling, and a semiconductor saturable absorber mirror (SESAM) for reliable operation at up to 300 mW output power and with a repetition rate of ~ 90 MHz. In the discussion of the experimental results we emphasize how spectral shaping can be used most efficiently in the generation of the shortest possible pulse supported by the Ti:sapphire gain bandwidth.

PACS: 42.55.Rz; 42.60.Fc; 42.65.Re; 42.79.Wc; 42.79.Bh; 85.30.De

Optical pulses in the two-cycle regime are attractive both because of their short temporal duration and because of their large spectral bandwidth. Previously, such pulses were only achievable by extracavity pulse compression [1, 2] or parametric amplification [3]. Both of these techniques rely on a white-light continuum that is produced using high-energy laser pulses. We have recently demonstrated that continuum-generation can be used directly inside an oscillator to extend continuous wave (cw) modelocked laser operation beyond the gain bandwidth leading to sub-6-fs pulses [4]. Morgner et al. reported equivalent pulse durations at a slightly longer center wavelength [5]. In comparison to the previous sources, the laser oscillator offers the advantage of a higher repetition rate at lower system complexity.

Fourier transform of the gain spectrum with its peak at 800 nm and its full-width at half-maximum (FWHM) of 200 nm [6] leads to an estimate of about 5 fs for the FWHM pulse duration τ_{FWHM} achievable with a Ti:sapphire laser. Self phase-modulation (SPM) can broaden the pulse bandwidth, and intracavity continuum generation beyond the gain bandwidth has been observed experimentally [4, 7]. While this suggests that theoretically even shorter pulses are feasible, dispersion compensation supporting the bandwidth needed for a sub-6-fs Ti:sapphire laser pulse is very challenging. After passing through 1 mm of sapphire, the relative group delay between wavelength components at 700 nm and 1 μm is 43 fs. Even for a very thin crystal, a sub-6-fs pulse will temporally stretch, and it will need to be compressed inside the resonator by one order of magnitude. Unfortunately, the chirped mirrors commonly used today typically show deviations from the desired group delay (T_{g}). These deviations tend to oscillate with wavelength and increase with the bandwidth of the mirrors [8].

In this paper, we describe the key components that allow us to obtain shaped pulse spectra with a transform-limit of $\tau_{\mathrm{FWHM}} < 5$ fs directly from a KLM Ti:sapphire laser. The laser employs broadband double-chirped mirrors (DCMs, [8–10]) for dispersion compensation and a broadband semiconductor saturable absorber mirror (SESAM, [11, 12]) to assist Kerr-lens modelocking. Spectral shaping is achieved with a custom-designed output coupling (OC) mirror [4, 13]. We show how amplitude and/or phase shaping can lead to a significant reduction of τ_{FWHM}. The laser performance is analyzed with phase-sensitive pulse diagnostics, and current limitations are pointed out.

1 Experimental results

A sketch of our laser resonator is shown in Fig. 1. The folded linear cavity has a round-trip cavity length of 3 m. It employs a SESAM at one end of the resonator and a custom-designed OC mirror as the second end mirror. All other mirrors are broadband DCMs from a single coating run. The laser crystal has a plane-to-plane thickness of 2.3 mm and a doping level of 0.25 wt.%. The maximum output power attained for the 5.8-fs pulse shown in Fig. 2 is 300 mW at an absorbed pump power of 4.7 W from a frequency-doubled, diode-pumped neodymium-vanadate laser (Spectra Physics Millennia-X). Other results presented here were obtained with an argon-ion pump laser (Coherent Innova 200), a slightly longer 92-MHz

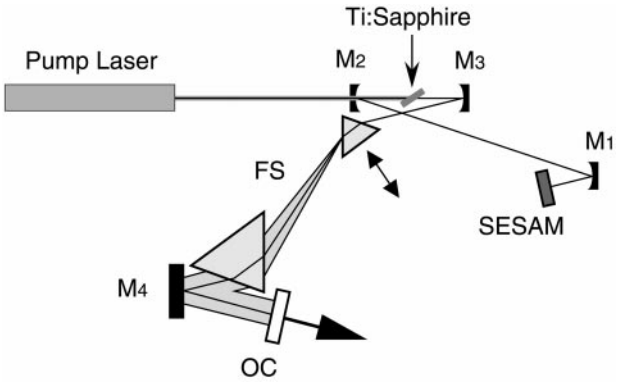

Fig. 1. Ti:sapphire laser resonator (M1–M4: double-chirped mirrors, OC: output coupling, FS: fused-silica prisms with 40 cm apex separation and variable material insertion, SESAM: semiconductor saturable absorber mirror). Extracavity, the spectrally dispersed output beam is recombined with an identical prism sequence, and the dispersion of the substrate of the output coupling mirror is compensated with seven additional reflections off double-chirped mirrors

cavity and a similar set of DCMs discussed below, but an otherwise unchanged configuration. Figures 2 and 3 show two sets of spectrum and autocorrelation measurements of this laser, achieved with the two different mirror sets. In both examples, pulse shaping via wavelength- dependent OC was employed as illustrated by the comparison of intracavity and extracavity spectra in Figs. 2a and 3a. The intracavity spectra of Figs. 2a and 3a support a transform-limited pulse duration of $\tau_{\mathrm{FWHM}} = 6.7$ fs and 6.8 fs, respectively, whereas the extracavity transform limit is 5.3 fs in both cases. In Fig. 2 the spectral phase retrieved from autocorrelation and spectrum yields $\tau_{\mathrm{FWHM}} = 5.8$ fs [4]; in Fig. 3 SPIDER (spectral phase interferometry for direct electric-field reconstruction) results in a 5.9 fs pulse duration [14]. The commonly used ideal sech^2 fit would have resulted in a severe underestimation of τ_{FWHM} (4.5 fs in Fig. 2b and 4.7 fs in Fig. 3b), due to the significant deviation from an ideal sech^2 spectrum in both cases. A sinc^2 assumption gives an improved estimate for τ_{FWHM}, Fig. 3b, but phase-sensitive diagnostics

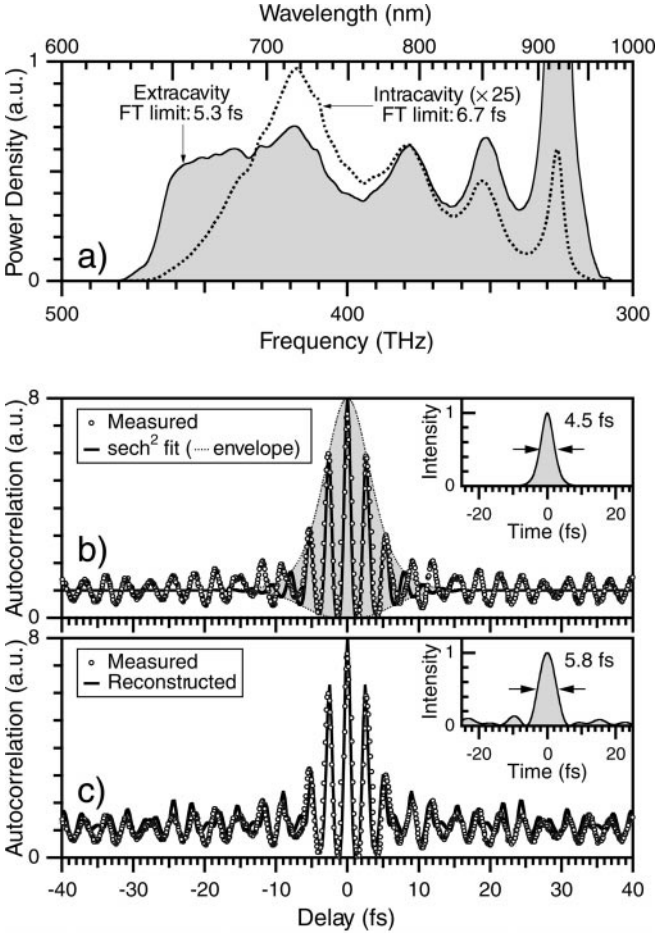

Fig. 2a–c. Sub-6-fs laser pulse: **a** Intracavity and extracavity pulse spectrum (spectral power density); **b** measured interferometric autocorrelation (*circles*) and calculated trace (*solid line*) that results from an ideal sech^2 fit, yielding a 4.5-fs pulse; **c** measured interferometric autocorrelation (*circles*) and calculated trace (*solid line*) that results from a fit to the extracavity spectrum and intensity autocorrelation [4]. The envelopes of the autocorrelation for the ideal sech^2 surround the shaded area. The *inset* in **c** shows the temporal intensity envelope resulting from the phase-retrieval algorithm. Its FWHM is $\tau_{\mathrm{FWHM}} = 5.8$ fs. The extracavity Fourier-transform (FT) limit of $\tau_{\mathrm{FWHM}} = 5.3$ fs is shorter than the intracavity value of $\tau_{\mathrm{FWHM}} = 6.7$ fs, due to spectral shaping via wavelength-dependent output coupling

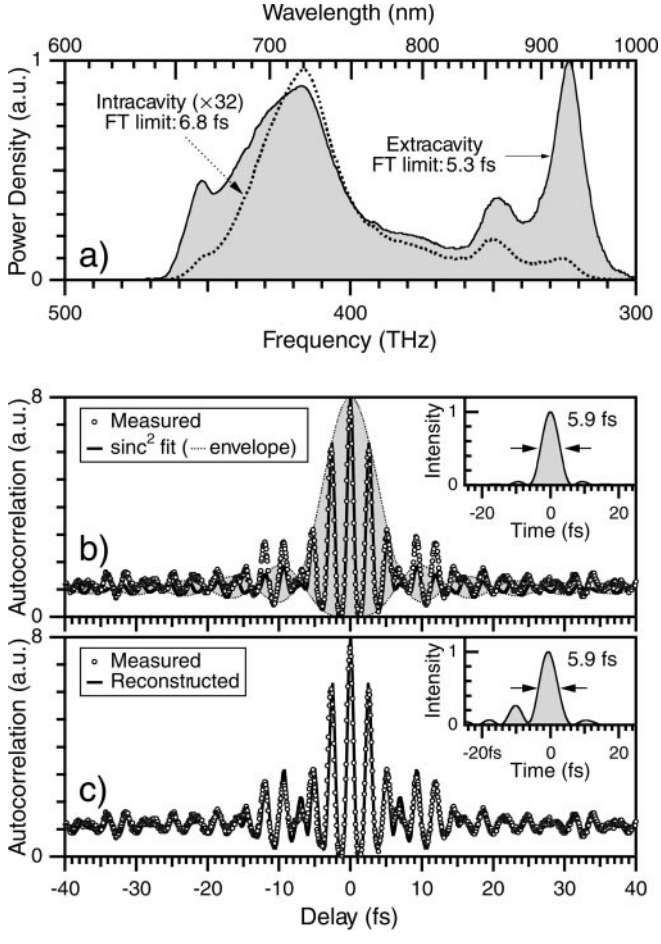

Fig. 3a–c. Sub-6-fs laser pulse: **a** Intracavity and extracavity pulse spectrum (spectral power density); **b** measured interferometric autocorrelation (*circles*) and calculated trace (*solid line*) that results from an ideal sinc^2 fit, yielding a 5.9-fs pulse; **c** measured interferometric autocorrelation (*circles*) and calculated trace (*solid line*) that results from phase-sensitive characterization with SPIDER [14]. The envelopes of the autocorrelation for the ideal sinc^2 surround the shaded area. A sech^2 assumption yields 4.7 fs (not shown). The *inset* in **c** shows the temporal intensity envelope retrieved with SPIDER. Its FWHM is $\tau_{\mathrm{FWHM}} = 5.9$ fs. The extracavity Fourier-transform (FT) limit of $\tau_{\mathrm{FWHM}} = 5.3$ fs is shorter than the intracavity value of $\tau_{\mathrm{FWHM}} = 6.8$ fs, due wavelength-dependent output coupling

obviously result in a much better agreement with the measured autocorrelation. Surprisingly, for both Figs. 2 and 3, the retrieved pulses are shorter than the intracavity transform limit. The key ingredients for the performance of the laser are the different types of mirrors, as discussed in the following.

2 Dispersion compensation with double-chirped mirrors (DCMs)

The DCMs are designed to provide dispersion compensation in conjunction with a standard fused-silica prism pair used for fine-tuning of the group-delay dispersion (GDD). The high-reflectance range of the DCMs covers the gain bandwidth of Ti:sapphire, significantly exceeding the performance of standard femtosecond coatings. Figure 4 illustrates how longer wavelengths penetrate deeper into the mirror structure and therefore experience a larger group delay upon reflection. The DCM coatings are fabricated with ion-beam sputtering (IBS). Together with online optical monitoring during the growth, this method gives very reproducible results [15].

For broadband DCMs, the GDD tends to oscillate around the desired target function (Fig. 5). This is mainly caused by the index discontinuity between air and the coating material [8]. One method to reduce this effect is the use of a second DCM with suitably shifted oscillations. Although it has been suggested that a pair of chirped mirrors with opposite oscillations should be designed in a single computer optimization process [16], we employ a similar but simpler method, utilizing non-normal incidence on a flat folding mirror to shift the residual GDD oscillation of the DCM coating. We carefully choose the angle of incidence for the best cancellation of the GDD oscillation. As shown in Fig. 5, this approach works well for most of the high-reflectance range of the mirrors.

3 Stabilization of Kerr-lens modelocking with a semiconductor saturable absorber mirror (SESAM)

We use a broadband SESAM with a low-finesse antiresonant Fabry–Pérot structure to stabilize Kerr-lens modelocking. The SESAM consists of a silver bottom mirror, followed by an AlAs spacer layer and the absorbing layers: a 20-nm $In_{0.22}Ga_{0.78}As$ quantum well (QW) sandwiched between GaAs layers, see Fig. 6a. The modulation depth due to bleaching of the absorption is $\Delta R \approx 3.5\%$ over a bandwidth of 400 nm, see Fig. 6b. The saturation fluence is $F_{A,sat} \approx 180\,\mu J/cm^2$ and the absorber recovery time is $\tau_A \approx 2$ ps (Fig. 7).

As compared to pure KLM, the cavity alignment and the starting of the pulsed operation are significantly simplified by using the SESAM. The laser runs for many hours, providing stable single-pulse operation in the two-cycle regime with little changes of power or pulse width. Moreover, KLM can be sustained over a wide range of the cavity parameters. Using SESAM-assisted KLM allows us to work in a region characterized by superior beam quality and higher average output power. This improvement of beam quality is most apparent in the extreme spectral wings (in our case below 650 nm), where the cavity can no longer provide sufficient spatial mode confinement, mainly due to the strongly reduced reflectance of the OC mirror. This is demonstrated in Fig. 8 which shows a comparison of transverse mode profiles in the yellow as observed behind one of the double-chirped resonator mirrors. The DCM coating has several sharp transmission resonances below 620 nm (Fig. 4) and blocks the main parts of the pulse spectrum, together with additional color filtering provided with laser safety goggles. After blocking the red and infrared components in the spectrally dispersed path between the external prisms, the yellow becomes visible also in the output beam.

4 Spectral shaping for the reduction of pulse durations

Haus' master equation predicts a hyperbolic secant temporal and spectral pulse shape for KLM lasers [17]. For sub-10-fs lasers, a refined model, based on dispersion-managed solitons, predicts Gaussian or super-Gaussian intracavity spectral shapes [18]. Measured pulse shapes in this regime, however, generally exhibit a more complex multi-peaked structure caused by small imperfections in dispersion compensation (Figs. 2a and 3a). In the following, we explore how spectral shaping can be used for the generation of the shortest pulses, and we discuss the implications for the extracavity pulse shape.

4.1 Wavelength-dependent output coupling (OC)

To optimize the performance of the laser, we have designed OC mirrors with different bandwidths and transmissions ranging from 2% to 8% (at 780 nm). Most of these designs are based on quarter-wave stacks, where the bandwidth is governed by the refractive index ratio of the dielectric coating materials. The target transmission of these designs are inversely proportional to Gaussians with transform limits of about 7 fs and centered near 800 nm, Fig. 9a. The reason for this becomes clear in Sect. 4.2. For broadband OC, a thin glass plate can be placed in one resonator arm with one side anti-reflection coated and the other side uncoated to yield Fresnel reflection. Under certain circumstances, this can lead to two outputs of the same spectrum but opposite chirp [19]. In the current work, we alternatively use a broadband OC mirror with a chirped dielectric coating. This mirror provides $\approx 5\%$ transmission from 650 nm to 1.1 μm (Fig. 9b).

4.2 Optimum amplitude shaping

Let us assume that the finite gain of Ti:sapphire and the finite bandwidth of the resonator mirrors support a maximum bandwidth of approximately 190 THz, beyond which the spectrum drops to zero. For example, this would correspond to a wavelength range from 650 nm to 1.1 μm. At pulse durations well above 10 fs, such spectral clipping does not result in any significant increase of pulse width. In contrast, a broad Gaussian amplitude spectrum with a FWHM of $\nu_{FWHM} = 100$ THz resulting in a transform-limit of 6.2 fs, is already stretched to $\tau_{FWHM} = 6.8$ fs with the 190 THz bandwidth limit.

Infinitely increasing the bandwidth of the Gaussian would result in a 190-THz broad box spectrum with a 4.7-fs Fourier limit. The duration can be decreased further by

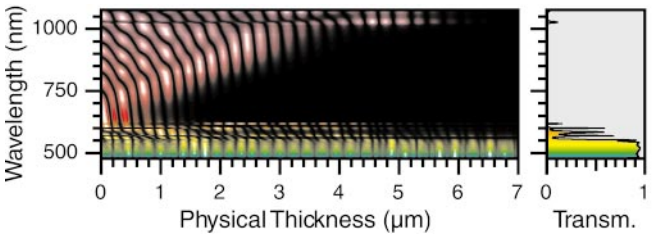

Fig. 4. Double-chirped mirror (DCM): normalized standing wave intensity distribution inside the DCM coating (image plot: brightness corresponds to intensity). In the high-reflectance band, longer wavelengths penetrate deeper into the coating. For the green pump light, the mirror has a high transmission (Transm.) as shown on the right plot

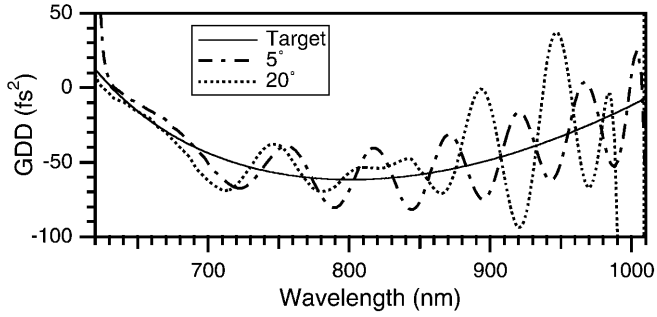

Fig. 5. Group-delay dispersion (GDD) of the double-chirped mirror for incidence angles of 5° (*dash-dotted*) and 20° (*dotted*), compared with the design target (solid line). The 20° angle is chosen for best cancellation of the GDD oscillation

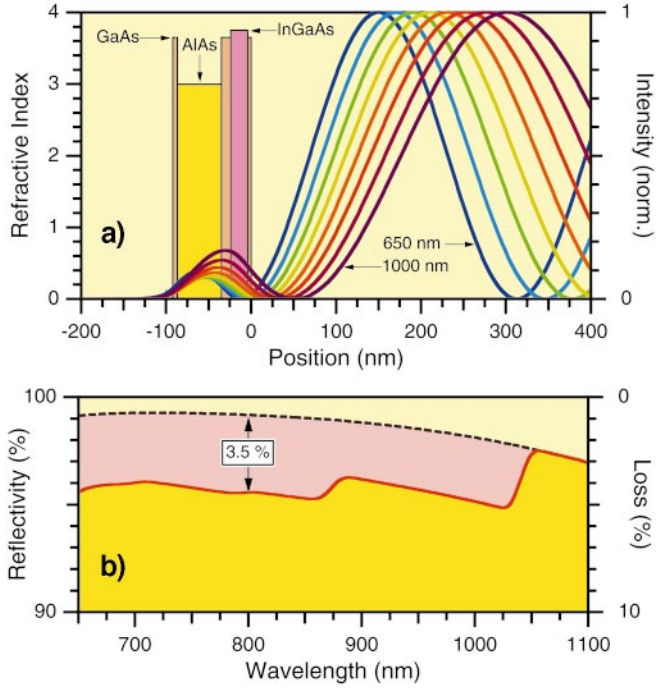

Fig. 6a,b. SESAM design: **a** normalized standing-wave intensity distribution for wavelengths from 650 nm to 1 μm and refractive index profile; **b** reflectivity in the unsaturated regime (low incident light intensity, *solid line*) and under saturation (e.g. for the short intracavity pulses, *dashed line*). The SESAM structure is designed to show a broadband saturable loss with a modulation depth of ≈ 3.5%, shaded in **b**

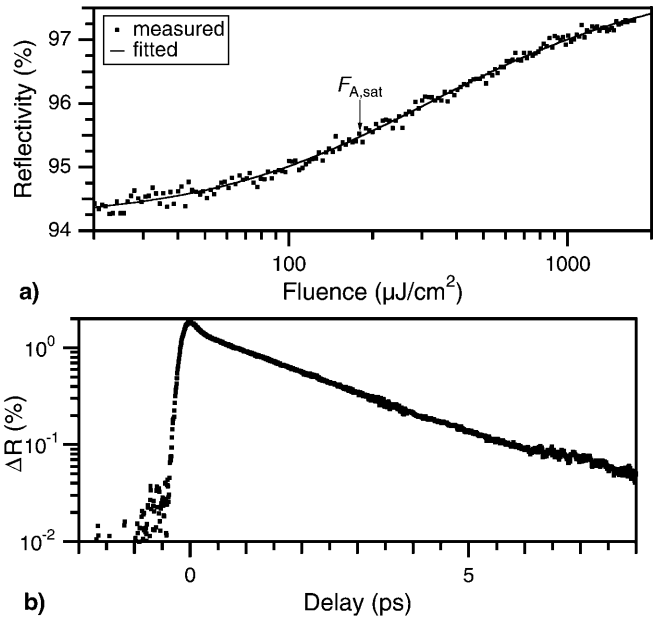

Fig. 7a,b. Absorption bleaching of the SESAM: **a** the measured saturation fluence is $F_{A,sat} = 180\,\mu J/cm^2$; **b** the modulation depth ΔR shows an exponential absorber recovery time of $\tau_A = 2$ ps in the pump-probe trace. Both measurements were done with 150-fs, 830-nm pulses from a Spectra-Physics Tsunami laser. The pump-probe trace was recorded at a pump fluence of 75 $\mu J/cm^2$ and a probe fluence of 3 $\mu J/cm^2$

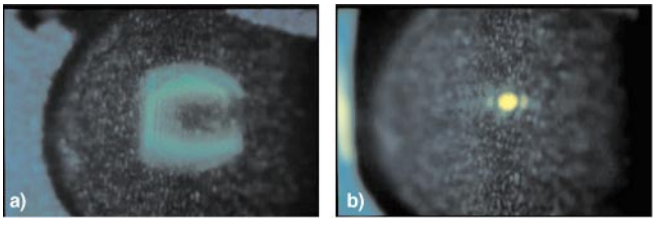

Fig. 8a,b. Transverse mode profiles observed on a screen behind resonator mirror M1 (Fig. 1): **a** with the resonator close to the stability limit, pure KLM action; **b** with resonator further away from the stability limit, SESAM-assisted KLM. Photographs taken with a 100ASA slide film (Kodak Elite) and laser safety goggles to suppress the red and infrared

lifting the spectral wings via wavelength-dependent output coupling [13], resulting in M-shaped spectra. However, this decrease of τ_{FWHM} is traded for increased pedestals or satellite pulses. Going to the extremes, strongly modulated spectra like those obtained recently from an impulsively excited Raman medium [20] correspond, under transform-limited conditions, to a train of extremely short pulses with a temporal spacing determined by the spectral modulation period.

So far, we have discussed spectral shaping in terms of τ_{FWHM}, which is a commonly used but somewhat arbitrary standard. The root-mean-square pulse duration τ_{rms}, i.e. the standard deviation of the temporal intensity envelope, is a more suitable criterion for the theoretical evaluation of pulse shapes. For spectral windowing as described above, τ_{rms} and therefore also the rms time–bandwidth product $\Delta\nu_{rms}\tau_{rms}$ are limited by τ_{rms} of the spectral windowing function. The largest possible curvature of the intensity envelope is determined by $\Delta\nu_{rms}$, i.e. the standard deviation of the spectral intensity, and will be reached at linear spectral phase [21].

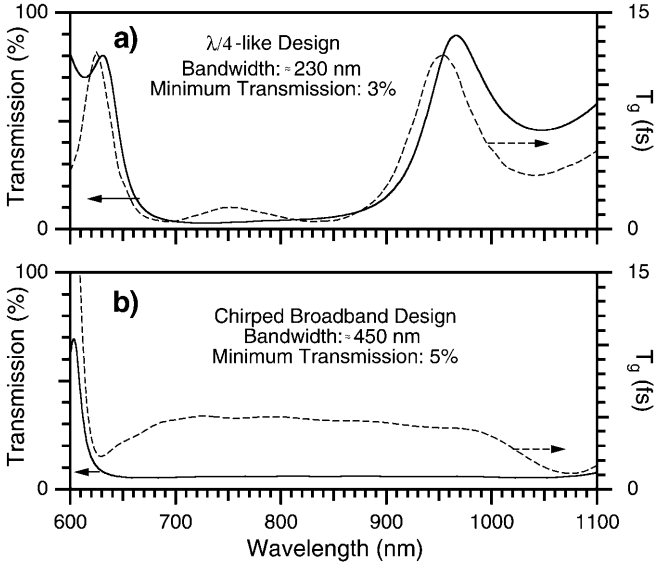

Fig. 9a,b. Output coupling and group delay upon transmission (T_g) of a commercially available quarter-wave-like ($\lambda/4$) coating (**a**, CVI Laser Corporation) and of a chirped, broadband coating designed for a 5% transmission over a bandwidth of more than 450 nm (**b**). For the $\lambda/4$ coating, T_g is qualitatively similar to the transmission characteristics

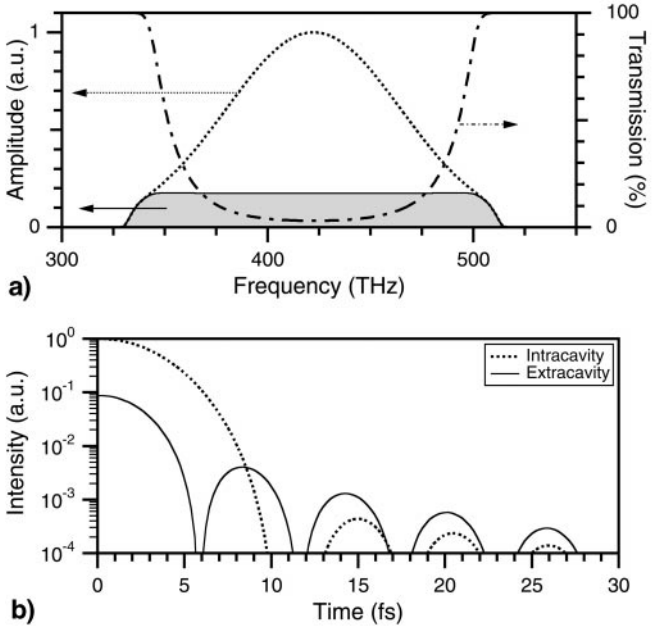

Fig. 10a,b. Ideal amplitude shaping by wavelength-dependent output coupling: **a** The intracavity amplitude spectrum (the square root of the spectral power density) is a Gaussian with a full-width at half-maximum bandwidth of $\nu_{\mathrm{FWHM}} = 100$ THz, clipped to 190 THz support (*dotted line*). A minimum transmission of 3% has been assumed. The external spectrum is box-shaped (*solid line*, *shaded*). **b** The semi-logarithmic plot of the temporal intensity envelope reveals sinc^2-like side peaks. The intracavity transform-limited pulse duration is $\tau_{\mathrm{FWHM}} = 6.8$ fs and the extracavity transform limit is $\tau_{\mathrm{FWHM}} = 5.1$ fs. The extracavity pulse power is 6.9% and the peak intensity 8.7% of the respective intracavity values

Such a pulse is termed "transform-limited" because a linear phase will also yield the smallest rms time–bandwidth product $\Delta\nu_{\mathrm{rms}}\tau_{\mathrm{rms}}$ if it exists at all. Note that τ_{rms} may not be defined for certain theoretical pulse shapes, for example for a sinc^2 function [21]. For some applications, the rise time of the pulse, or the contrast ratio between peak and background intensity, the autocorrelation width, or the smoothness of the pulse spectrum might be more important criteria. Spectral shaping can be employed to improve either of these properties.

A practical compromise between τ_{FWHM} and pulse quality is given by a box-shaped spectrum with a sinc^2 temporal intensity profile. Such a spectrum is achieved when the OC is inversely proportional to the intracavity power spectrum. This neglects the influence of the OC on the intracavity pulse formation, which is a good approximation as long as the intracavity spectral width is limited mainly by the gain bandwidth. The maximum relative increase of power in the spectral wings is given by $1/T_{\mathrm{min}}$, where T_{min} is the minimum transmission of the OC mirror. For the quarter-wave-like mirror designs, Sect. 4.1, we assumed intracavity spectra similar to those obtained with previous broadband DCMs [19]. In the example shown in Fig. 10, shaping a clipped Gaussian spectrum into a box results in a reduction of τ_{FWHM} to 75% of its intracavity value. However, it has to be noted that amplitude shaping is always accompanied by phase effects, as explained by the Kramers–Kronig relations that prohibit pure amplitude shaping, and additional phase compensation is required to fully exploit this reduction of τ_{FWHM}.

4.3 Optimum phase shaping

The largest peak-to-average intensity ratio will be reached for transform-limited pulses. It is possible, however, that deviations from a linear phase reduce τ_{FWHM} below the transform-limited value (Fig. 11). In this case, more pronounced temporal pedestals arise and the rms duration τ_{rms} is increased. At

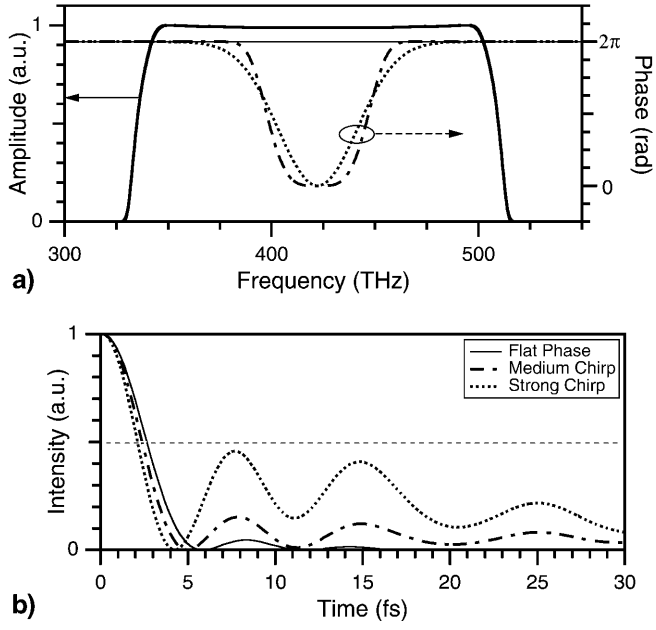

Fig. 11a,b. Phase shaping: **a** The box-shaped spectrum of Fig. 2a is Fourier-transformed assuming a constant phase (*solid line*) and with two different non-constant phases (*dash-dotted*: medium chirp, *dotted*: strong chirp). **b** The temporal intensity envelope shows increasing side-peaks at decreasing peak intensity. The pulse duration is $\tau_{\mathrm{FWHM}} = 5.1$ fs at flat spectral phase, 4.6 fs at medium chirp, and 4.0 fs at strong chirp. Normalized to the same average power, the peak intensity for medium chirp is 58% of the transform-limited pulse and 34% for strong chirp

the same time, the peak intensity drops, and the instantaneous frequency becomes time-dependent, inducing a chirp on the pulse.

KLM lasers rely on the quasi-instantaneous self-amplitude modulation (SAM) of the Kerr-lens inside the crystal. Together with unbalanced dispersion and spectral shifts due to SPM, SAM causes spectral amplitude shaping. Strong shaping due to unbalanced fourth-order dispersion has been described previously [22, 23]. In fully dispersion-compensated linear resonators, a Fourier-limited pulse is obtained in the center of the gain crystal and at the end mirrors of the resonator if the dispersion is equally distributed on both resonator arms [5]. This results in optimum SAM and consequently in shortest intracavity pulses. We therefore designed our laser to provide equal negative group delay dispersion (GDD) in both arms [4].

Because the pulse is theoretically transform-limited at the end of the resonator, the extracavity pulse will consequently carry a chirp induced by the transmission through the OC mirror. For the maximum attainable extracavity peak intensity, phase shaping has to be employed to remove this chirp. Currently, we use DCMs and prisms for this purpose. The potential of liquid crystal devices that allow for both amplitude and phase shaping [24, 25] needs further experimental analysis.

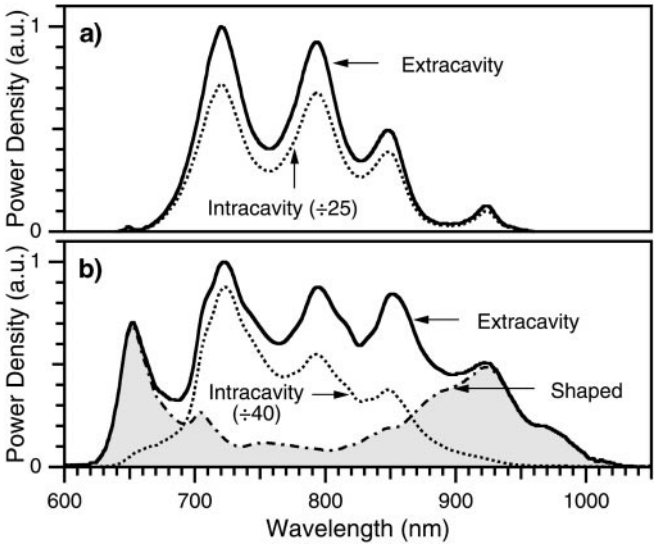

Fig. 12a,b. Extracavity (*solid lines*) and intracavity (*dotted lines*) spectral power density for a pulse obtained **a** with 5%-transmission of 450-nm bandwidth and **b** with 3%-transmission of 230-nm bandwidth. In **a** the intracavity peak intensity is lower than in **b** due to higher output coupling and a longer pulse duration. In **a** the transform-limit is $\tau_{\mathrm{FWHM}} = 7.7$ fs for both spectra, in **b** it is 6.9 fs for the intracavity pulse and 5.3 the extracavity pulse. The dash-dotted spectrum in **b** is obtained by additional spectral shaping of the extracavity pulse and has a transform-limit of 4.5 fs

5 Pulse characterization

Spectral shaping, together with the combination of linear and nonlinear processes inside the cavity, gives rise to complex pulse shapes, that require advanced pulse characterization tools. Techniques such as FROG (frequency-resolved optical gating, [26, 27]) and SPIDER [28, 29] measure amplitude and phase. If these methods are unavailable, autocorrelation and spectrum provide useful information that can be extracted with suitable algorithms [30]. After a study of the observed pulse spectra and autocorrelations we discuss the results of SPIDER measurements. For a comparison of methods for the sub-10-fs range, including a detailed description of SPIDER and collinear FROG, the reader is referred to [31].

5.1 Spectrum

With the 450-nm bandwidth OC, Fig. 9b, we observe nearly identical intra- and extracavity spectra, both with a transform limit of $\tau_{\mathrm{FWHM}} = 7.7$ fs (Fig. 12a). In Fig. 12b, shaping with an OC mirror of 230-nm bandwidth is demonstrated. The transmission is larger in the spectral wings, and the transform- limited pulse duration drops from 6.9 fs for the intracavity pulse to 5.3 fs for the extracavity pulse. The same OC has been used in Fig. 1. That observed pulse spectra extend into the yellow, Fig. 8, is a clear indication of strong SPM inside the Ti:sapphire crystal and can be interpreted as intracavity white-light generation [7]. As the yellow light cannot extract additional gain from the laser medium, it is most efficiently used with maximum OC. The spectra shown in Fig. 12a exhibit stronger amplitude modulation than those of Fig. 12b, indicative of weaker SAM due to a lower intracavity peak intensity. The modulation of the spectrum stems from the residual oscillation of the intracavity GDD [23].

The third spectrum displayed in Fig. 12b has a Fourier limit of 4.5 fs. This spectrum has been obtained with additional external amplitude shaping. Insertion of thin copper wires into the spectrally dispersed output beam causes diffraction losses for particular spectral components. As explained in Sect. 4.2, this should allow for a shorter τ_{FWHM}, but due to uncompensated phase contributions, we did not succeed in generating a shorter autocorrelation. Larger pedestals observed in the autocorrelation measurements are a side effect of this shaping.

5.2 Interferometric autocorrelation (IAC)

Traditionally, the interferometric or fringe-resolved autocorrelation (IAC) has been the most widely accepted standard for pulse characterization. To extract the pulse width from the autocorrelation, a model function is assumed for the pulse shape and both the carrier frequency and the width are fitted [32]. If the shape of the pulse is known, its width will be directly proportional to the autocorrelation width.

An unchirped sech^2 shape has been frequently used to evaluate autocorrelations of passively modelocked lasers. For spectra that are closer to a box-shape than to a sech^2, pre- and post-pulses lead to wings in the IAC. In such cases, a sech^2 assumption will only fit to the central fringes of the IAC and the true pulse width can be severely underestimated, Sect. 1, Fig. 2. A sinc^2 assumption has been used to obtain a more realistic estimate of the real pulse duration [5]. However, for M-shaped spectra as obtained [5] and for other pulse shapes that have significant pre- and/or post pulses (see Figs. 10 and 11), a sinc^2 assumption can lead to an underestimation of the pulse width. In Fig. 13, fitting an ideal sinc^2 pulse to the IAC resulting from an M-shaped spectrum yields $\tau_{\mathrm{FWHM}} = 5.5$ fs. This corresponds to a 5% underestimation of

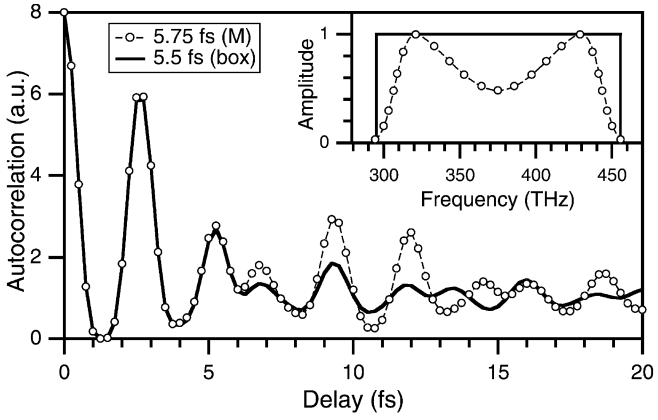

Fig. 13. The M-shaped amplitude spectrum shown in the inset (*circles*) results in a transform-limited 5.75-fs pulse with the interferometric autocorrelation shown in the main plot (*circles*). A fit to this autocorrelation assuming an unchirped sinc^2 pulse yields the *solid line*, which corresponds to the box-shaped spectrum (*solid line*) in the *inset* and a pulse duration of 5.5 fs

the pulse width, in spite of the excellent agreement in the central fringes of the IACs. This illustrates that the information in the wings of the autocorrelation must not be discarded in the decorrelation process.

Although autocorrelations do contain information about the pulse shape in addition to the pulse width, a simple guess of pulse shape and chirp introduces a severe uncertainty in the determination of the pulse width. To reduce this uncertainty, additional information is required. For the IAC shown in Fig. 2 we have used an iterative algorithm that allows for a phase reconstruction from autocorrelation and spectrum without an a priori assumption of a particular pulse shape [1, 30]. The retrieved 5.8-fs pulse duration is 10% longer than the transform limit. As the algorithm uses only the dc part of the IAC, a comparison of reconstructed and measured IAC provides an independent test of the result. The retrieved phase, however, still depends on how the squared deviation between measured and retrieved autocorrelation is weighted. For a more accurate determination from autocorrelation and spectrum, a high-dynamic-range intensity autocorrelation would be required.

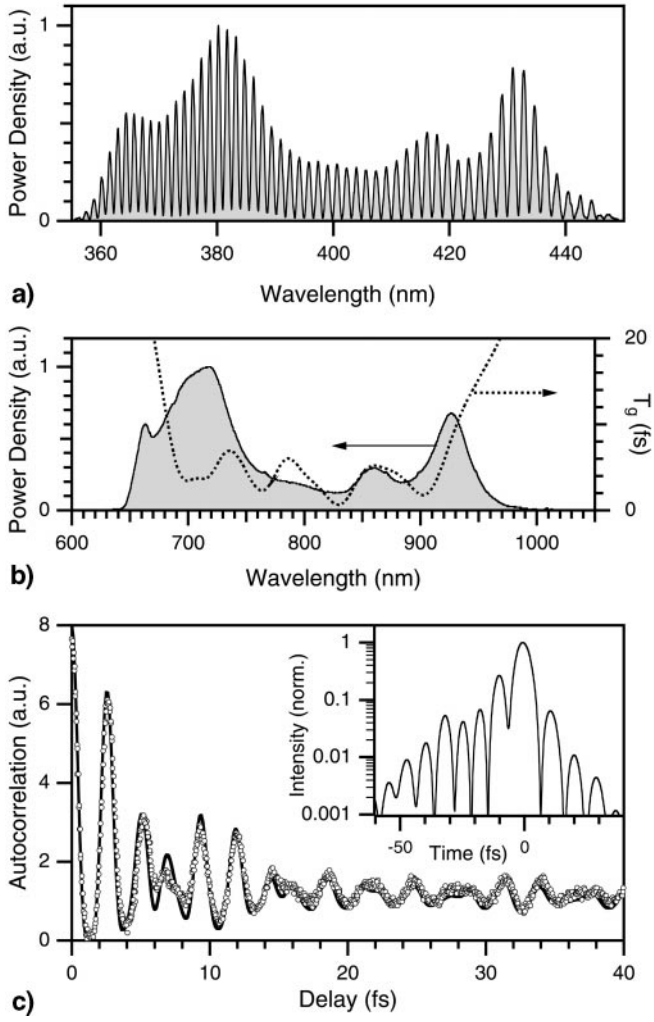

Fig. 14. a SPIDER trace: spectral interference pattern between the two upconverted sheared spectra; **b** retrieved phase and spectrum; **c** measured autocorrelation (*dots*) compared with the one calculated from retrieved pulse (*solid line*). For display purposes, we use the absolute value of the time delay. The measured pulse duration is $\tau_{\mathrm{FWHM}} = 5.9$ fs, and the transform-limit is 5.3 fs. The *inset* in **c** shows the retrieved temporal pulse envelope revealing pedestals on a semi-logarithmic plot

5.3 Spectral phase interferometry for direct electric-field reconstruction (SPIDER)

For a full characterization of the pulses, we chose a SPIDER version that was specifically designed for sub-10-fs pulses [14]. In the SPIDER apparatus, a pair of identical replicas of the pulse, slightly delayed in time with respect to another, are spectrally sheared by upconversion. From the interference of the sheared spectra, Fig. 14a, the phase of the original pulse can be deduced by a simple, non-iterative algorithm.

From the retrieved spectral phase the spectral group delay is calculated, as shown in Fig. 14b. The corresponding pulse (inset of Fig. 3c) has a duration of $\tau_{\mathrm{FWHM}} = 5.9$ fs, which is 11% above the transform-limited value of 5.3 fs but 15% shorter than the transform-limit of the intracavity spectrum. In this example, shaping has been used to increase the spectrum on the long-wavelength side, with an OC mirror transmission 14 times larger for 930 nm than for 720 nm. This leads to a strongly M-shaped external spectrum, Figs. 3a and 14b.

To provide a cross-check between the different measurement techniques, we reconstructed the IAC trace from the SPIDER data. A comparison with the independently measured IAC is shown in Fig. 14c. Great care was taken to compensate for the different path lengths in air between the laser and the two diagnostic measurement set-ups. With the retrieved SPIDER data, we have simulated the influence of spectral shaping in our autocorrelator, caused by color filter glasses (Schott BG3, BG38, BG39) and second-harmonic conversion efficiency (10-μm ADP crystal, cut for 800-nm SHG), on the IAC. We find that such filtering introduces no significant systematic errors in our IAC measurement. The deviation between the two traces in Fig. 14b is very small, confirming the excellent agreement of our diagnostic methods.

The retrieved group delay in Fig. 14b exhibits small oscillations with a rms amplitude of 1.5 fs between 690 nm

and 920 nm, which stems from the residual dispersion oscillation of the DCMs. Outside this range, the group delay increases rapidly. This has to be compared with the characteristics of a typical quarter-wave OC mirror shown in Fig. 9a, which exhibits a nearly constant group delay between 700 nm and 900 nm. Outside this range, the group delay roll-off is qualitatively similar to the one observed with SPIDER. We therefore attribute the measured group delay to the effect of both the OC coating and the DCMs used for external dispersion compensation. Mirror coatings could, in principle, be designed to compensate for the diverging group delay in the high-transmittance region of the OC coating. However, it is not reasonable to fabricate new high-reflecting mirrors for every kind of OC mirror that could possibly be used. Alternatively, adaptive phase control has been demonstrated for longer pulses, and is certainly attractive for use with pulses in the few-cycle regime.

6 Conclusion

We have obtained sub-6-fs pulses directly from a SESAM-assisted KLM Ti:sapphire laser. Our results show that spectral shaping provides an efficient way to produce shorter pulses and to extend the spectrum of the modelocked pulses beyond the gain bandwidth. With the yellow light generated in our laser, we have a clear indication of intracavity white-light continuum generation. We have carefully characterized our pulses with SPIDER and determined durations below the intracavity Fourier transform limit. The small residual chirp can be attributed mainly to the dispersion of the OC mirror. As pointed out in Sect. 4.3 (Fig. 11), phase shaping could even be used to push τ_{FWHM} below the extracavity transform limit. Using the entire gain bandwidth of Ti:sapphire, an intracavity 5.5-fs pulse appears to be achievable. Similar spectral shaping would then result in a sub-4-fs pulse. This clearly demonstrates that, even with the pulses reported in this paper, there is still some potential for shorter pulses and the ultimate limit for Ti:sapphire lasers has not yet been reached. A remaining challenge in this regime is the reduction of dispersion oscillations and the compensation of the external phase.

The wide frequency combs of ultrafast pulses allow for new applications in precision frequency metrology. Based on the ocatave-spanning spectra of two-cycle pulses, novel schemes have been proposed which give access to a measurement of the carrier-envelope offset (CEO) phase φ_{CEO} [33]. Controlling φ_{CEO}, a predicted phase dependence of nonlinear optical processes can be explored, which is expected to be significant only at pulse durations of two cycles or below. The scope of new applications clearly motivates the quest for shorter and shorter pulses.

Acknowledgements. The authors thank T. Groß and D. Ristau, Laserzentrum Hannover, for supplying a variety of custom-made output coupling mirrors, and M. Haiml, ETH Zurich, for measuring recovery time and saturation fluence of the SESAM. This work has been supported by the Swiss National Science Foundation.

References

1. A. Baltuska, Z. Wei, M.S. Pshenichnikov, D.A. Wiersma, R. Szipöcs: Appl. Phys. B **65**, 175 (1997)
2. M. Nisoli, S. Stagira, S.D. Silvestri, O. Svelto, S. Sartania, Z. Cheng, M. Lenzner, C. Spielmann, F. Krausz: Appl. Phys. B **65**, 189 (1997)
3. A. Shirakawa, I. Sakane, M. Takasaka, T. Kobayashi: Appl. Phys. Lett. **74**, 2268 (1999)
4. D.H. Sutter, G. Steinmeyer, L. Gallmann, N. Matuschek, F. Morier-Genoud, U. Keller, V. Scheuer, G. Angelow, T. Tschudi: Opt. Lett. **24**, 631 (1999)
5. U. Morgner, F.X. Kärtner, S.H. Cho, Y. Chen, H.A. Haus, J.G. Fujimoto, E.P. Ippen, V. Scheuer, G. Angelow, T. Tschudi: Opt. Lett. **24**, 920 (1999)
6. P.F. Moulton: J. Opt. Soc. Am. B **3**, 125 (1986)
7. J.P. Likforman, A. Alexandrou, M. Joffre: Appl. Phys. Lett. **73**, 2257 (1998)
8. N. Matuschek, F.X. Kärtner, U. Keller: IEEE J. Sel. Top. Quantum Electron. **4**, 197 (1998)
9. F.X. Kärtner, N. Matuschek, T. Schibli, U. Keller, H.A. Haus, C. Heine, R. Morf, V. Scheuer, M. Tilsch, T. Tschudi: Opt. Lett. **22**, 831 (1997)
10. N. Matuschek, F.X. Kärtner, U. Keller: IEEE J. Quantum Electron. **QE-35**, 129 (1999)
11. R. Fluck, I.D. Jung, G. Zhang, F.X. Kärtner, U. Keller: Opt. Lett. **21**, 743 (1996)
12. I.D. Jung, F.X. Kärtner, N. Matuschek, D.H. Sutter, F. Morier-Genoud, Z. Shi, V. Scheuer, M. Tilsch, T. Tschudi, U. Keller: Appl. Phys. B **65**, 137 (1997)
13. D.H. Sutter, I.D. Jung, F.X. Kärtner, N. Matuschek, F. Morier-Genoud, V. Scheuer, M. Tilsch, T. Tschudi, U. Keller: IEEE J. Sel. Top. Quantum Electron. **4**, 169 (1998)
14. L. Gallmann, D.H. Sutter, N. Matuschek, G. Steinmeyer, U. Keller, C. Iaconis, I.A. Walmsley: Opt. Lett. **24**, 1314 (1999)
15. M. Tilsch, V. Scheuer, J. Staub, T. Tschudi: SPIE Conf. Proc. **2253**, 414 (1994)
16. V. Laude, P. Tournois: In Conference on Lasers and Electro-Optics (CLEO '98), CTuR4 (1999)
17. H.A. Haus, J.G. Fujimoto, E.P. Ippen: IEEE J. Quantum Electron. **QE-28**, 2086 (1992)
18. U. Morgner, F.X. Kärtner, Y. Chen, S.H. Cho, H.A. Haus, J.G. Fujimoto, E.P. Ippen: In Ultrafast Optics 1999, Technical Digest, paper Tu8 (1999)
19. D.H. Sutter, I.D. Jung, N. Matuschek, F. Morier-Genoud, F.X. Kärtner, V. Scheuer, M. Tilsch, T. Tschudi, U. Keller: In Ultrafast Phenomena XI, Vol. 63 (Springer, Berlin, Heidelberg 1998) p. 11
20. A. Nazarkin, G. Korn, M. Wittmann, T. Elsaesser: Phys. Rev. Lett. **83**, 2560 (1999)
21. R.N. Bracewell: *The Fourier Transform and Its Applications* (McGraw-Hill, New York 1986)
22. I.P. Christov, M.M. Murnane, H.C. Kapteyn, J. Zhou, C.P. Huang: Opt. Lett. **19**, 1465 (1994)
23. A. Rundquist, C. Durfee, Z. Chang, G. Taft, E. Zeek, S. Backus, M.M. Murnane, H.C. Kapteyn, I. Christov, V. Stoev: App. Phys. B **65**, 161 (1997)
24. D. Meshulach, D. Yelin, Y. Silberberg: Opt. Commun. **138**, 345 (1997)
25. T. Baumert, T. Brixner, V. Seyfried, M. Strehle, G. Gerber: Appl. Phys. B **65**, 779 (1997)
26. D.J. Kane, R. Trebino: IEEE J. Quantum Electron. **QE-29**, 571 (1993)
27. R. Trebino, K.W. DeLong, D.N. Fittinghoff, J. Sweetser, M.A. Krumbügel, B. Richman: Rev. Sci. Instrum. **68**, 1 (1997)
28. C. Iaconis, I.A. Walmsley: Opt. Lett. **23**, 792 (1998)
29. C. Iaconis, I.A. Walmsley: IEEE J. Quantum Electron. **QE-35**, 501 (1999)
30. J. Peatross, A. Rundquist: J. Opt. Soc. Am. B **15**, 216 (1998)
31. L. Gallmann, D.H. Sutter, N. Matuschek, G. Steinmeyer, U. Keller: Appl. Phys. B, Suppl. to **70**, 67 (2000)
32. J.-C. Diels, J.J. Fontaine, I.C. McMichael, F. Simoni: Appl. Opt. **24**, 1270 (1985)
33. H.R. Telle, G. Steinmeyer, A.E. Dunlop, J. Stenger, D.H. Sutter, U. Keller: Appl. Phys. B **69**, 327 (1999)